Actin disassembly clock determines shape and speed of lamellipodial fragments

Noa Ofer[a], Alexander Mogilner[b,c], and Kinneret Keren[a,d,1]

[a]Department of Physics and the Russell Berrie Nanotechnology Institute, Technion-Israel Institute of Technology, Haifa 32000, Israel; [b]Department of Neurobiology, Physiology, and Behavior, University of California, Davis, CA 95616; [c]Department of Mathematics, University of California, Davis, CA 95616; and [d]Network Biology Research Laboratories, Technion-Israel Institute of Technology, Haifa 32000, Israel

Edited by James A. Spudich, Stanford University School of Medicine, Stanford, CA, and approved October 3, 2011 (received for review April 14, 2011)

A central challenge in motility research is to quantitatively understand how numerous molecular building blocks self-organize to achieve coherent shape and movement on cellular scales. A classic example of such self-organization is lamellipodial motility in which forward translocation is driven by a treadmilling actin network. Actin polymerization has been shown to be mechanically restrained by membrane tension in the lamellipodium. However, it remains unclear how membrane tension is determined, what is responsible for retraction and shaping of the rear boundary, and overall how actin-driven protrusion at the front is coordinated with retraction at the rear. To answer these questions, we utilize lamellipodial fragments from fish epithelial keratocytes which lack a cell body but retain the ability to crawl. The absence of the voluminous cell body in fragments simplifies the relation between lamellipodial geometry and cytoskeletal dynamics. We find that shape and speed are highly correlated over time within individual fragments, whereby faster crawling is accompanied by larger front-to-rear lamellipodial length. Furthermore, we find that the actin network density decays exponentially from front-to-rear indicating a constant net disassembly rate. These findings lead us to a simple hypothesis of a disassembly clock mechanism in which rear position is determined by where the actin network has disassembled enough for membrane tension to crush it and haul it forward. This model allows us to directly relate membrane tension with actin assembly and disassembly dynamics and elucidate the role of the cell membrane as a global mechanical regulator which coordinates protrusion and retraction.

cell motility | keratocyte fragments

Understanding the large-scale coordination of molecular processes into coherent behavior at the cellular level is one of the central challenges in cell biology. Actin-based motility involves numerous molecular players with complex interactions (1) that span a wide-range of scales from the molecular level to the cellular one. Despite substantial progress in characterizing the molecular details involved (2), we still do not understand the remarkable self-organization of these molecular components into a moving cell. The complex interplay between biochemical reactions and biophysical forces plays a central role in this self-organization. In particular, the mechanical feedback between the cell membrane and the dynamic actin network has been shown to have a substantial effect on cell protrusion (3, 4), and a significant role in coordinating protrusion over cellular scales (5, 6). However, quantitative understanding of the coupling between the cell membrane and the motility machinery is still lacking; it is unknown what determines membrane tension and how membrane tension is related to the protrusion and retraction dynamics. Elucidating this dynamic interplay is essential for understanding how overall cell morphology and movement emerge from the underlying molecular processes.

Fish epithelial keratocytes are widely used for studying the dynamics of the motility process (5, 7–10); they are one of the fastest moving animal cells with average speeds of up to 1 μm/s, yet their motion is extremely persistent with hardly any change in cell shape, speed, or direction over many minutes. Keratocytes, as well as other motile cell types (11), can spontaneously detach cytoplasmic fragments which move with speed and persistence similar to whole-cells (12–14). These lamellipodial fragments, which lack nuclei, microtubules, and most organelles, are likely the simplest natural model system for studying actin-based cell motility. As such, this system has been used to gain insight into the minimal requirements for establishing polarity in motile cells (12, 13). Here we utilize this simplified model system to study how the interplay between actin dynamics and the plasma membrane lead to shape and movement of the lamellipodium as a whole. The lack of a cell body in fragments facilitates measurements of geometry and movement of the rear boundary, allowing us to focus on the important question of how retraction at the rear is coordinated with protrusion at the front.

We combine experimental characterization and modeling and propose a self-consistent biophysical model of the lamellipodial motility module. We show that membrane tension mechanically couples edge dynamics along the cell boundary; at the rear, membrane tension provides the force needed for retraction and actin network disassembly, whereas a force balance between actin polymerization and membrane tension shapes the leading edge (5). Overall, our model explains in a quantitative and self-consistent manner how global shape and speed of the lamellipodium emerge from the underlying dynamics of the actin treadmill within an inextensible membrane bag, and provides values for membrane tension as an output of the model rather than incorporating tension as an input parameter.

Results

Keratocyte Fragments as a Model System for Lamellipodial Motility. Lamellipodial fragments are naturally produced at low frequency in keratocyte cultures and remain viable for hours. By inducing fragment formation (see *Materials and Methods*), a large population of fragments can be obtained from primary keratocyte cultures (Fig. 1). The fragment population exhibits substantial morphological variability, similar to that seen in a population of whole-cells (5) (Fig. 1*A*). The spectrum of shapes can be described to a large extent (~90%) by two orthogonal shape modes (Fig. 1*B*). Roughly, these modes can be described as measuring the projected area (mode 1), and the front-to-rear lamellipodial length (mode 2). Fragments are typically smaller than cells, and their movement is somewhat slower (Fig. S1).

The actin network organization in fragments (13, 14) is similar to that found in whole keratocytes (5, 9). Along the leading edge,

Author contributions: N.O. and K.K. designed research; N.O. and K.K. performed research; A.M. contributed new reagents/analytic tools; N.O., A.M., and K.K. analyzed data; and N.O., A.M., and K.K. wrote the paper.

The authors declare no conflict of interest.

This article is a PNAS Direct Submission.

See Commentary on page 20275.

[1]To whom correspondence should be addressed. E-mail: kinneret@physics.technion.ac.il.

This article contains supporting information online at www.pnas.org/lookup/suppl/doi:10.1073/pnas.1105333108/-/DCSupplemental.

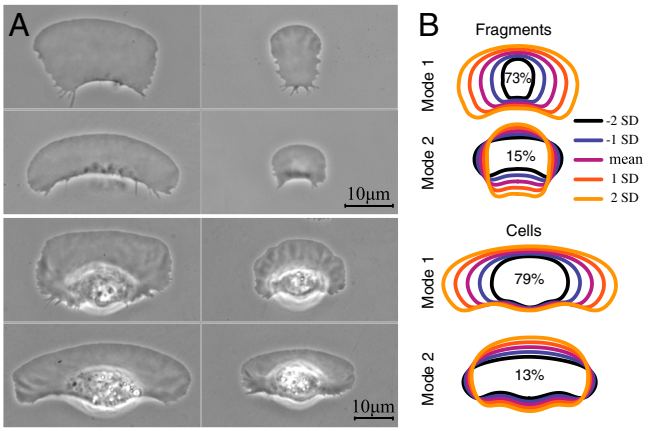

Fig. 1. Fragment shape and movement resembles that of whole keratocytes. (*A*) Phase-contrast images of live fragments (*Top*) and whole keratocytes (*Bottom*) are shown. Fragments exhibit a similar spectrum of lamellipodial shape variation as cells. (*B*) The first two principal modes of shape variation, as determined by principal components analysis of aligned outlines of 122 live fragments (*Top*) and 148 cells (*Bottom*), are shown. Essentially the same modes—cell area (Mode 1) and front-to-rear lamellipodial length (Mode 2)—are found for both fragments and cells. These two modes capture approximately 90% of the shape variation in the populations. For each mode, the mean cell shape is shown together with reconstructions of shapes one and two standard deviations away from the mean in each direction along the given mode. The variation accounted for by each mode is indicated.

the actin filament density is peaked at the center and decreases toward the sides (Fig. 2 *A* and *B*) as in cells (5, 8). Perpendicular to the leading edge, the network density is highest near the leading edge and decreases approximately exponentially toward the rear (Fig. 2*C*) (13, 14). Measurements of the actin network dynamics in fragments using quantitative fluorescent speckle microscopy (15) show that the network is nearly stationary in the lab frame of reference, and hence flows rearward in the cell frame of reference (Fig. 2 *D–E*, Movie S1). Similar flow patterns were observed in whole keratocytes, with the important difference that in whole-cells a myosin II-dependent inward actin flow was prominent near the rear boundary (7, 16). This difference is likely due to the higher quantity of myosin II in cells (9) compared to fragments (13), which are typically generated from lamellipodia that are relatively poor in myosin (9). Importantly, myosin appears to be dispensable for steady-state fragment motility as myosin inhibition with blebbistatin has essentially no effect on fragment shape or speed (Fig. 2*F*).

Together, the observations that (*i*) the actin network density decays approximately exponentially as a function of distance from the leading edge, and (*ii*) the actin network remains nearly stationary with respect to the substrate, imply that the treadmilling actin network exhibits net disassembly at a constant rate per unit time (*SI Text*). We measure this disassembly rate by combining time-lapse microscopy of live fragments with rapid fixation and staining of the actin network within the same fragments (Fig. 2 *G* and *H*, Movie S2). The disassembly time is equal to the ratio between the decay length of the actin density from front-to-rear (Fig. 2*G*) and fragment speed. We find an average disassembly time of 30 ± 12 s (mean $\pm$ standard deviation, $N = 11$; Fig. 2*H*), which is comparable with the relevant data for cells (17). The disassembly time varies widely (over threefold) between different fragments (Fig. 2*H*), likely reflecting cell-to-cell variability in the concentration of proteins such as actin depolymerizing factor (ADF)/cofilin involved in actin disassembly.

Different cells or fragments may possess varying amounts of specific proteins, lipids, or other materials, but the biochemical and biophysical rules governing the interactions of those constituents are the same. Thus, characterization of the natural pheno-

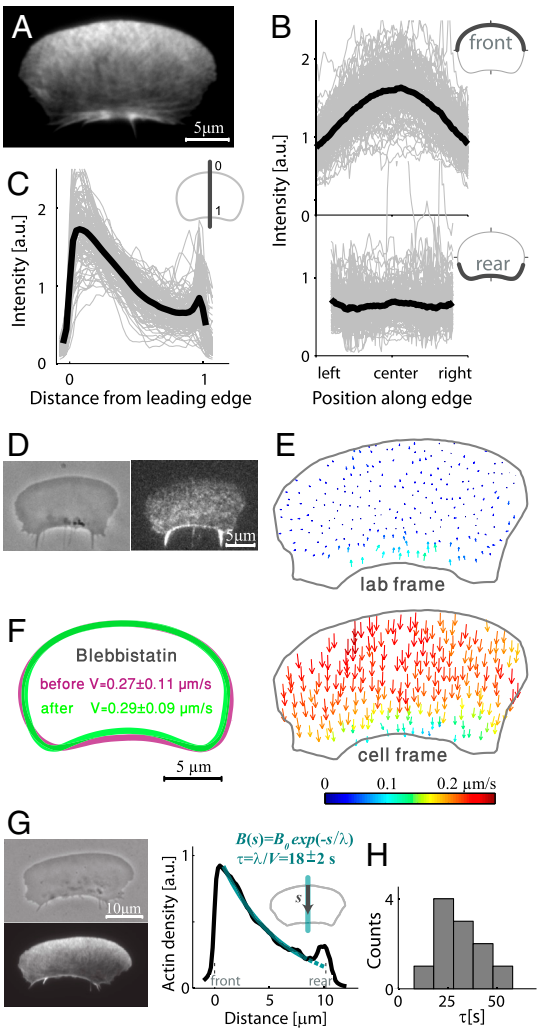

Fig. 2. Actin organization and dynamics in fragments. (*A*) A fluorescence image of a fragment which was fixed and stained with fluorescent phalloidin to visualize actin filament distribution. (*B–C*) The filament distribution was measured for a population of fixed fragments ($N = 115$). Data for individual fragments normalized to the mean intensity within that fragment (gray lines) is shown together with the population average (black). (*B*) The actin filament density profile along the leading edge (*Top*) and trailing edge (*Bottom*) are shown. The intensity is plotted as a function of the relative position along the boundary. The filament density along the leading edge is peaked at the center, whereas the density along the trailing edge is essentially flat. (*C*) The density along a cross section perpendicular to the leading edge is plotted as a function of the normalized distance from the leading edge (front-to-rear distance = 1). The actin filament density is peaked near the leading edge and decreases toward the rear. (*D*) Phase-contrast and fluorescence images of a fragment labeled with low levels of fluorescent phalloidin (Movie S1). (*E*) Actin network flow maps obtained by fluorescent speckle microscopy for the fragment shown in *D* are depicted in the lab frame of reference (*Top*) and in the cell frame of reference (*Bottom*). The magnitude of the flow is indicated by both the length and the color of the flow vectors. The actin network is nearly stationary in the lab frame of reference, and exhibits rearward flow within the lamellipodium in the cell frame of reference. (*F*) Myosin inhibition by blebbistatin has little effect on fragment shape and speed. The average shape and speed for a population of fragments ($N = 40$) before and after treatment with blebbistatin are depicted. (*G*) A phase-contrast image (*Upper Left*) from a time-lapse movie of a live fragment and a fluorescence image (*Lower Left*) of the same fragment after fixation and phalloidin staining are shown (Movie S2). The actin network density along a cross section from front-to-rear (*Right*) is well-fit by an exponential function with the decay length as a fit parameter. The characteristic actin disassembly time (equal to the model parameter τ) is measured as the ratio between the decay length of the actin density and fragment speed. (*H*) A histogram of the characteristic actin disassembly times measured as in *G* for a population of fragments ($N = 11$).

typic variation across a population reveals the spectrum of possible functional states of the system, and has led to substantial insights into the mechanism of shape determination in motile keratocytes (5, 8). However, variation within a population (e.g., in the actin disassembly rate as shown above) can mask important correlations. In particular, although speed is perhaps the most fundamental characteristic of motile cells, previous work failed to find a tight connection between speed and morphology. To overcome this difficulty we focus on variations within individual fragments over time. We expect the biochemical composition of fragments to remain nearly constant on the relatively short timescales considered here (seconds to several minutes). The extent of variation in speed and morphology in fragments during this time frame is substantially smaller than the variation within a population (Fig. S2). Nonetheless, as shown below, following the dynamics within individual fragments and in particular the correlation between speed and morphology over time allows us to gain unique insight into the system, regardless of the cell-to-cell variability.

Fragment Shape and Speed Vary in a Correlated Manner over Time. To identify characteristic features in individual fragments that correlate with motility, we use high-resolution time-lapse microscopy (Movies S3 and S4) to quantify the morphology and speed of motile fragments over time. We find that the area of individual fragments remains remarkably stable over time (Fig. S2), suggesting that the total area of the plasma membrane is constant and that the membrane is stretched taut by the expanding actin network. This notion is further supported by perturbation experiments in which fragments are treated with high osmolarity medium and their area remains unchanged (Fig. S3).

Importantly, we find that speed and front-to-rear lamellipodial length are strongly correlated within individual fragments over time (Fig. 3): As fragments slow down their front-to-rear distance decreases, whereas faster movement is accompanied by larger front-to-rear distance. Furthermore, we find that changes in leading edge protrusion speed precede changes in the front-to-rear distance by a few seconds, whereas changes in the speed of the trailing edge tend to follow changes in the front-to-rear distance (Fig. 3*D*). Similar correlations are observed in whole keratocytes (Fig. S4), indicating that the same mechanisms govern movement of fragments and cells.

The correlation between front-to-rear lamellipodial length and speed is suggestive of an actin disassembly clock mechanism (18) in which the front-to-rear distance is defined by the time needed for the actin network to disassemble to the point where membrane tension can crush the weakened network at the rear. According to this model the front-to-rear distance will scale as fragment speed multiplied by the time needed for sufficient network disassembly, so the front-to-rear distance is predicted to correlate with speed (Fig. 3 *B* and *C*). Furthermore, changes in front-to-rear distance are expected to follow changes in actin assembly (and hence speed) at the leading edge, whereas the rear is expected to react to these changes with a delay, as observed (Fig. 3*D*). As described below, the actin disassembly clock model can be formulated mathematically and yields a self-consistent set of equations that define fragment shape and speed as well as membrane tension.

Disassembly Clock Model Predicts Fragment Shape, Speed, and Membrane Tension. We consider a treadmilling actin network within an inextensible membrane bag and assume local force balance between the forces imposed by the motility machinery from within and those generated by the surrounding membrane (Fig. 4). Because membrane tension equilibrates rapidly, we assume that tension is spatially homogenous along the boundary (5, 19). The lamellipodial rear is defined by where the force needed to retract the rear is equal to the force generated by membrane tension. We

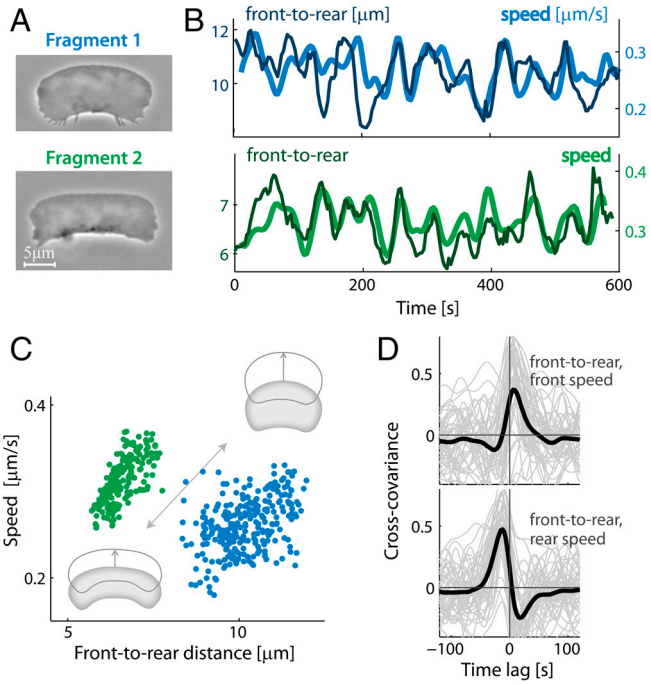

Fig. 3. Fragment shape and speed vary in a correlated manner. Forty-five fragments were followed over >10 min at 3 s time intervals. Data is shown for two typical fragments (Movies S3 and S4). (*A*) Phase-contrast images of the fragments. (*B*) Traces of the front-to-rear distance and speed over time for both fragments show clear temporal correlation. (*C*) Scatter plots of speed as a function of front-to-rear distance for the two fragments are shown. Larger front-to-rear distance correlates with faster movement. (*D*) The normalized cross-covariance between the front-to-rear distance and the speed of the leading edge (*Top*) and between the front-to-rear distance and the speed of the trailing edge (*Bottom*) are depicted as a function of time lag for individual fragments (gray lines). The mean cross-covariance functions averaged over all 45 fragments are also shown (black lines).

make the simplest assumptions that the resistance to rear retraction is mainly due to the actin network and that the strength of the actin network is proportional to its density. Under these assumptions, the force needed to retract the rear boundary is linearly proportional to the local network density there. Along the leading edge, the force imposed by the membrane is distributed locally among the pushing filaments (4), so the load force per filament is equal to the tension divided by the local filament density (5). The value of the membrane tension is a dynamic variable which depends on the spatio-temporal organization of the actin network and at the same time influences it. At steady-state, the membrane tension is determined self-consistently by the system.

The disassembly clock model can be made quantitative by coupling the force-density relations for actin polymerization at the leading edge and disassembly at the rear (Fig. 4, *SI Text*). We consider a two-dimensional model, denoting the front-to-rear distance (at the center) y and the side-to-side distance $2x$ (Fig. 4*A*). Because fragments are approximately rectangular, we estimate the total length of the front and sides of the leading edge by $2L = 2(x + y)$ and area by $A = 2xy$. The actin filament density along the leading edge has an approximately parabolic distribution, peaked at the center (Fig. 2*B*, Fig. S5). Thus, we express the filament density distribution by $B(l) = B_C(1 - l^2/L^2)$, where l is the position along the leading edge ($l = 0$ at the center) and B_C is the actin filament density at the center of the leading edge (5, 8, 20). We assume that the front corners, which form the boundary between the protruding leading edge and the stalled sides, are defined by where the load force per filament reaches the stall force for polymerization (21). The force imposed by the membrane tension, T, is then equal to the stall force per filament

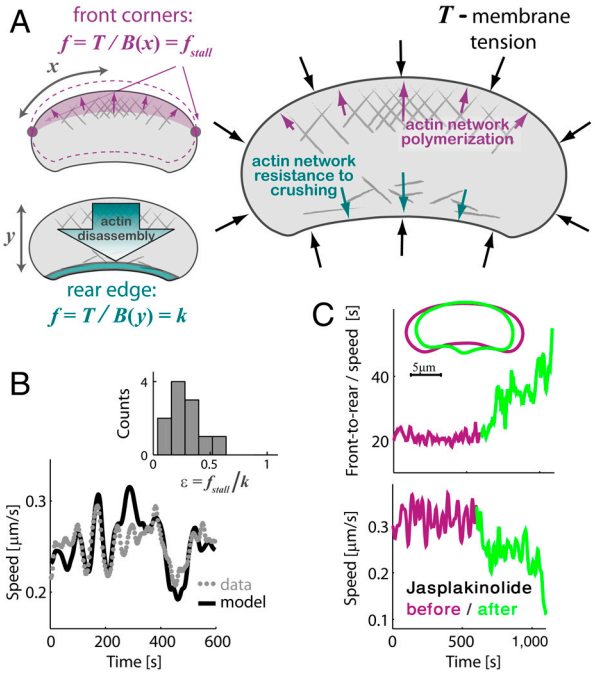

Fig. 4. The disassembly clock model. (*A*) A schematic illustration of the two-dimensional disassembly clock model. Membrane tension generates a constant force per unit length along the perimeter. At the front corners, the force per filament, which is equal to the membrane tension divided by the local filament density, reaches the stall force. Along the rear boundary, the force needed to crush the network is equal to the membrane tension. (*B*) Speed as a function of time is depicted for the fragment shown in Fig. 2*G* (gray points). The data is well-fit by the model prediction, $V(t) = \frac{y(t)}{\tau}\left\{\frac{-1}{\log\varepsilon + \log[1-(1+2y(t)^2/A)^{-2}]}\right\}$, using the measured actin disassembly time τ and area A for this fragment (black line). The data and model prediction are smoothed with $\sigma = 6$ s and the best-fit ε is determined for each fragment. (*Inset*) A histogram of the values of the model parameter ε obtained from fitting the speed as a function of time for individual fragments ($N = 11$) is shown. The mean value $\varepsilon \sim 0.3$ agrees with an independent estimate for ε extracted from the actin distribution in fixed fragments (Fig. S7). (*C*) The effect of jasplakinolide treatment on fragments. The speed and front-to-rear displacement time (equal to the front-to-rear distance divided by speed) are depicted as a function of time for a fragment before and after adding jasplakinolide to the media. As predicted by the disassembly clock model, the front-to-rear displacement time, which is nearly constant prior to the perturbation, increases following the addition of jasplakinolide to the media, whereas speed decreases in response to the perturbation. (*Inset*) The mean shape of the fragment before and after treatment (averaged over 5 min). Similar results were obtained for four different jasplakinolide-treated fragments.

multiplied by the filament density at the corners (5): $T = f_{\text{stall}}B(x)$. We can express this force balance by an equation relating cell geometry (front-to-rear distance, y) and mechanics (membrane tension, T):

$$1 - \left(\frac{1}{1 + 2y^2/A}\right)^2 = \frac{T}{f_{\text{stall}}B_C}. \qquad [1]$$

Both the front-to-rear distance and membrane tension are unknown variables in Eq. **1**. We obtain another independent relation between these two variables by considering the force balance at the rear. The actin network disassembles at a constant rate $1/\tau$, where τ is the characteristic disassembly time. For a fragment moving at a speed V, the constant disassembly rate translates into an exponential decrease in filament density as a function of distance from the leading edge, s, so that: $B(s) = B_C \exp(-s/V\tau)$ (*SI Text*). The rear edge is defined as where the membrane-imposed force reaches the threshold force per filament needed to crush the actin network (break filaments and/or detach crosslinking and adhesion proteins associated with them) denoted by k. The force balance relation at the rear boundary ($s = y$) is hence given by, $T = kB(y)$, which can be rewritten as:

$$\exp\left(-\frac{y}{V\tau}\right) = \frac{f_{\text{stall}}}{k}\frac{T}{f_{\text{stall}}B_C} = \varepsilon\frac{T}{f_{\text{stall}}B_C}, \qquad \varepsilon = \frac{f_{\text{stall}}}{k}. \qquad [2]$$

Because membrane tension is uniform along the boundary (5, 19), the disassembly clock model predicts that the actin density along the rear edge will be approximately constant. Indeed, whereas the actin density profile along the leading edge is peaked, the measured profile along the rear boundary is flat (Fig. 2*B*), lending further support to the model. Note that an alternative model in which the rear boundary is shaped by a force balance between contractility of the actin-myosin bundle at the rear and membrane tension (19, 22) (Fig. S6) is inconsistent with our data: Myosin inhibition with blebbistatin leads to essentially no shape change and in particular no change in rear shape (Fig. 2*F*).

Together, Eq. **1** and Eq. **2** self-consistently determine both fragment shape and membrane tension. By combining them, we obtain an equation that determines the front-to-rear distance:

$$\exp\left(-\frac{y}{V\tau}\right) = \varepsilon[1 - (1 + 2y^2/A)^{-2}]. \qquad [3]$$

The stall force per filament is expected to be smaller than the force required to break a filament, so we expect, $\varepsilon = \frac{f_{\text{stall}}}{k} < 1$. Eq. **3** has a simple approximate solution for $\varepsilon << 1$: $V \approx \frac{y}{\tau}\cdot\left(\frac{-1}{\log\varepsilon}\right)$. More precisely we obtain $V = \frac{y}{\tau}\left\{\frac{-1}{\log\varepsilon + \log[1-(1+2y^2/A)^{-2}]}\right\}$ (*SI Text*). Fitting the last formula to the V vs. y time series for individual fragments, using the measured values for the area A and actin disassembly time τ for each fragment, gives excellent results and allows estimating ε in each fragment (Fig. 4*B*). We find that ε has a mean value of $\varepsilon = 0.3 \pm 0.15$ (mean $\pm$ standard deviation, $N = 11$; see also Fig. S7), so we predict that the breaking force per filament is approximately three times greater than the stall force, which is approximately 2–3 pN (21). Furthermore, we can use the model to estimate the membrane tension in each fragment; taking typical values we find $T \sim 150$–300 pN/μm (*SI Text*).

The disassembly clock model can be further tested by modifying actin dynamics in live cells with pharmacological agents and observing the concurrent changes in morphology and speed. Jasplakinolide is a cell-permeable drug which stabilizes actin filaments and slows their disassembly (23). Jasplakinolide-treated fragments exhibit a decrease in speed and an increase in the front-to-rear displacement time (y/V, i.e., the time it takes the front to reach the rear boundary) (Fig. 4*C*), as expected from the disassembly clock model for increased values of τ. Inhibition of the actin nucleator Arp2/3 (24) which decreases actin filament density at the leading edge leads to the expected reduction in speed (Fig. S8*C*). Arp2/3 inhibition also significantly slows down actin disassembly (Fig. S8 *A* and *B*), most likely due to the structural changes in the actin network. As a result, and in accordance with the disassembly clock model, we also observe an increase in the front-to-rear displacement time (Fig. S8*C*).

The detailed fragment shape, and in particular the curvature of the leading edge, can be predicted from the model if we incorporate a force-velocity relation for actin-network polymerization. Experimentally, we find that the leading edge curvature is highly correlated with the front-to-rear distance (Fig. 5, Fig. S4). Measurements of the force-velocity relation of protruding actin networks in the lamellipodium of motile keratocytes (25) have shown that protrusion is more sensitive to load at higher forces; at weak loads protrusion is nearly insensitive to force, whereas at greater loads, approaching the stall force, speed decreases rapidly. Spe-

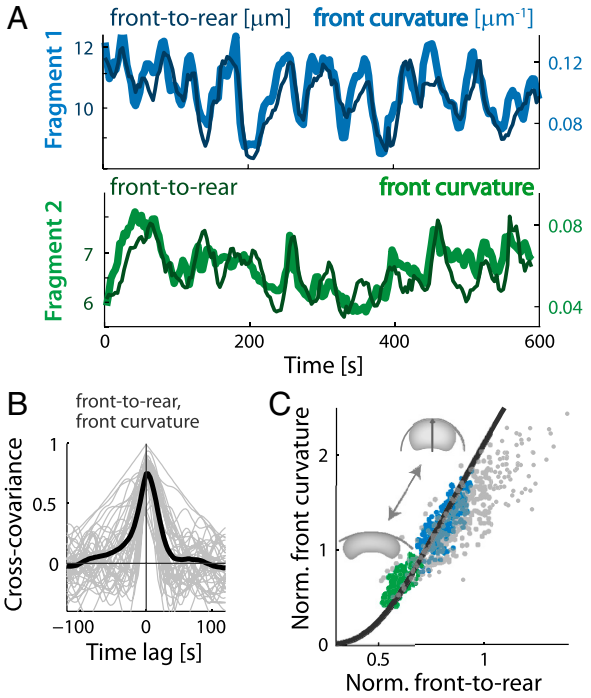

Fig. 5. The disassembly clock model predicts correlation between curvature of the leading edge and front-to-rear distance. (*A*) Traces of the front-to-rear distance and the curvature of the leading edge over time are depicted for the two fragments shown in Fig. 3*A*. The front-to-rear distance is correlated with the curvature of the leading edge. (*B*) The normalized cross-covariance between the front-to-rear distance and the front curvature is depicted as a function of time lag for individual fragments (gray lines), together with the mean cross-covariance function averaged over all 45 fragments (black line). (*C*) The normalized front curvature is shown as a function of the normalized front-to-rear distance. Normalization is done using the square root of fragment area as the length unit. Data is depicted for the time series of the two fragments shown in Fig. 3*A* (blue and green, respectively) and for a population of live fragments (gray). The data is well-fit by the predictions of the disassembly clock model (black lines).

cifically, we assume that the force-velocity relation is given by $V(f) = V_0\left[1 - \left(\frac{f}{f_{\text{stall}}}\right)^w\right]$, where V_0 is the free polymerization rate and $w = 8$. From the density distribution of actin filaments along the leading edge $B(l)$, we can estimate the local force per filament $f(l) = T/B(l)$. Based on the force-velocity relation, we obtain the local protrusion rate $V(l)$, which according to the graded radial extension model (5, 10) defines the shape of the leading edge (*SI Text*). Qualitatively, larger front-to-rear distance correlates with an increase in the load force per filament due to membrane tension at the leading edge (Eq. **1**). At larger front-to-rear distances and higher loads, the local protrusion rate becomes more sensitive to changes in the load force due to the laterally decreasing actin network density along the leading edge. According to the graded radial extension model (5, 10), this higher sensitivity implies that the curvature of the leading edge will increase. The model-predicted correlation between front-to-rear distance and curvature of the leading edge is in excellent agreement with the observed curvature-distance correlations both in a population and within individuals over time (Fig. 5*C*, Fig. S9).

Discussion

Through extensive analysis of the correlated behavior of individual fragments over time, we developed an essentially complete model of this autonomous motility module consisting of an actin network treadmilling within an inextensible membrane bag. The relative simplicity of fragments enabled us to reveal phenomena that are hidden or obscured in more complex model systems. Moreover, focusing on the behavior of individuals allowed us to observe correlations that would otherwise be masked by the natural cell-to-cell variability. Our self-consistent model couples global mechanical regulation by membrane tension with the self-organized dynamics of the actin network yielding testable predictions which are in quantitative agreement with our experimental results (Figs. 3–5).

Fragments exhibit actin assembly at the front and disassembly at a constant rate away from the leading edge. Shape and speed of the leading edge are determined by a force balance between the collective pushing of the polymerizing actin filaments and the load imposed by the membrane (Fig. S10*A*). At the sides, actin filament density is lower so protrusion is stalled by the membrane load. Finally, the actin network at the rear, weakened by disassembly processes and dissociation of various actin-binding and adhesion proteins, is crushed by membrane tension leading to rear retraction (Fig. S10*B*). Altogether, membrane tension, which is dynamically determined by the system, couples protrusion at the front with retraction at the rear with an actin disassembly clock setting the front-to-rear distance. Analogous actin dynamics with assembly at the front and disassembly at a constant rate characterize comet-tail motility (26) in which comet-tail length is proportional to speed due to a similar disassembly clock mechanism. However, in the absence of a surrounding membrane, the mechanical coupling between actin assembly and disassembly is lacking in comet tails.

The actin monomer concentration and the density of filaments at the leading edge are taken as constant model parameters. We speculate that the semioscillatory dynamics we observe in fragment shape and speed are related to changes in these parameters over time. In the *SI Text* we present a model which incorporates these parameters as dynamic variables and illustrates how lamellipodial shape and actin organization can self-organize and evolve into a unique stable asymmetric state. Future modeling should incorporate explicitly the spatio-temporal dynamics of actin assembly and disassembly processes, including actin filament nucleation, growth and capping, ADF-cofilin-induced filament breaking and Arp2/3 detachment, as well as thymosin and profilin monomer shuttling (2).

This work highlights the role of membrane tension in rear retraction, which naturally leads to mechanical coupling between retraction and protrusion. Myosin contraction can contribute to rear retraction as well as promote motility by enhancing actin disassembly (7) and inducing forward directed fluid flow (27). However, it is not required; knockouts and inhibition experiments have shown that although myosin II typically promotes movement and increases cell speed, it is not essential for motility in many cell types including keratocytes (5, 7, 27), *Acanthamoeba* (28), and *Dictyostelium discoideum* (29). Here we show that myosin II has a negligible role in rear retraction in keratocyte fragments (Fig. 2*F*). These results also imply that myosin is not essential for building a minimal actin-based artificial moving cell; membrane tension is sufficient for inducing rear retraction and coordinating protrusion and retraction.

Different combinations of redundant motility modules can explain all known modes of cell locomotion (30), and it is important to characterized each of these modules. We focus here on the basic actin treadmill in a membrane bag module which plays a central role in lamellipodial fragments and whole keratocytes (2, 9). Experimental evidence in more complex cells suggests that this basic module participates in their motile behavior as well: Switching off certain pathways converts the stubby and short uropod of *Dictyostelium* into a flat keratocyte-like rear (31), whereas the extended and long tail characteristic of motile fibroblasts often snaps also becoming a keratocyte-like rear (32). Moreover, upon myosin inhibition, spreading fibroblasts acquire a C-like shape, with a convex edge that protrudes and stretches the membrane, and a concave edge that is retracted by the

tension generated in the membrane (33), similar to what we observe in motile fragments.

Additional modules, most prominently adhesion- and signaling-related, are known to play important roles in more complex cells (34). Adhesion is obviously essential for lamellipodial motility. Moreover, recent evidence suggests that the balance between adhesion and contraction significantly affects cell shape and motile behavior in whole keratocytes (6). Although we do not incorporate adhesion dynamics explicitly here, adhesion assembly and turnover are strongly coupled to actin dynamics so the net actin disassembly rate incorporated in our model likely depends on adhesion turnover as well (35, 36) (Fig. S11). The role of biochemical signaling modules in fragments and whole keratocytes is still unclear. Our results indicate that the lamellipodium is self-organizing, rather than being organized by signals from the cell body (which is absent in fragments). However, biochemical signaling within the lamellipodium may still play a role in shaping actin assembly and disassembly dynamics.

The importance of mechanical forces and feedbacks in cell biology in general and in cell motility in particular is becoming apparent. However, quantitative understanding of the interplay between mechanical forces and biochemical processes in the cell remains an outstanding challenge. Our work presents an important step forward in this respect; we integrate membrane mechanics with actin dynamics into a single self-consistent biophysical model of lamellipodial motility which is in excellent quantitative agreement with the experimental data. Membrane tension equilibrates rapidly across the cell and provides essentially instantaneous coupling between actin assembly and disassembly events occurring at distal locations along the cell boundary through the mechanical loads imposed by the plasma membrane. In this manner, membrane tension acts as a global mechanical regulator of actin dynamics, effectively coordinating molecular processes over cellular scales. Such mechanical feedbacks provide rapid and robust means for communication at the cellular level and likely play an important role in many other cellular processes.

Materials and Methods

Primary cultures are prepared from the Central American cichlid *Hypsophrys nicaraguensis* as described previously (5, 8). Sheets of keratocytes are detached from the substrate by treatment with 0.1% trypsin (Gibco BRL) and replated onto a new coverslip. Cell fragment formation is induced by incubation in 1 mL of culture media supplemented with 100 nM staurosporine (Sigma) at 35 °C for 30 min with the lid half open. Live cell imaging is performed on glass-bottom petri dishes (fluorodish; World Precision Instruments Ltd.) at room temperature on a Zeiss Axio-Observer inverted microscope and acquired with a CoolSnap HQ2 CCD camera (Photometrics) using a 63× objective (N.A. = 1.4). Actin dynamics are measured as in ref. 7, and actin distribution is measured by fixation and phalloidin staining as in ref. 5. Quantitative image analysis is done using the cell-tool package developed by Pincus and coworkers (5, 37), and custom code written in Python and Matlab. Further details on the materials and methods used can be found in the *SI Materials and Methods*.

ACKNOWLEDGMENTS. We thank Zach Pincus for help with analysis using the cell-tool package and comments on the manuscript. We thank Cyrus Wilson and Gaudenz Danuser for providing the MatLab code used to track actin network movement in motile fragments. We thank Erez Braun, Erin Barnhart, Patricia Yam, Greg Allen, Michael Kozlov, Aretha Fiebig, and Yariv Kafri for fruitful discussions and comments on the manuscript. This work was supported by a Levi Eshkol fellowship from the Israel Science Ministry (N.O.), a European Research Council starting grant and Marie Curie International Reintegration Grant from the European Research Council (K.K.), a grant from the United States-Israel Binational Science Foundation (K.K. and A.M.), and by National Institutes of Health Grant GM068952 (to A.M.).

1. Ridley AJ, et al. (2003) Cell migration: Integrating signals from front to back. *Science* 302:1704–1709.
2. Pollard TD, Borisy GG (2003) Cellular motility driven by assembly and disassembly of actin filaments. *Cell* 112:453–465.
3. Raucher D, Sheetz MP (2000) Cell spreading and lamellipodial extension rate is regulated by membrane tension. *J Cell Biol* 148:127–136.
4. Schaus TE, Borisy GG (2008) Performance of a population of independent filaments in lamellipodial protrusion. *Biophys J* 95:1393–1411.
5. Keren K, et al. (2008) Mechanism of shape determination in motile cells. *Nature* 453:475–480.
6. Barnhart EL, Lee KC, Keren K, Mogilner A, Theriot JA (2011) An adhesion-dependent switch between mechanisms that determine motile cell shape. *PLoS Biol* 9:e1001059.
7. Wilson CA, et al. (2010) Myosin II contributes to cell-scale actin network treadmilling through network disassembly. *Nature* 465:373–377.
8. Lacayo CI, et al. (2007) Emergence of large-scale cell morphology and movement from local actin filament growth dynamics. *PLoS Biol* 5:e233.
9. Svitkina TM, Verkhovsky AB, McQuade KM, Borisy GG (1997) Analysis of the actin-myosin II system in fish epidermal keratocytes: Mechanism of cell body translocation. *J Cell Biol* 139:397–415.
10. Lee J, Ishihara A, Theriot JA, Jacobson K (1993) Principles of locomotion for simple-shaped cells. *Nature* 362:167–171.
11. Keller HU, Bessis M (1975) Migration and chemotaxis of anucleate cytoplasmic leukocyte fragments. *Nature* 258:723–724.
12. Euteneuer U, Schliwa M (1986) The function of microtubules in directional cell movement. *Ann NY Acad Sci* 466:867–886.
13. Verkhovsky AB, Svitkina TM, Borisy GG (1999) Self-polarization and directional motility of cytoplasm. *Curr Biol* 9:11–20.
14. Okeyo KO, Adachi T, Hojo M (2009) Dynamic coupling between actin network flow and turnover revealed by flow mapping in the lamella of crawling fragments. *Biochem Biophys Res Commun* 390:797–802.
15. Danuser G, Waterman-Storer CM (2006) Quantitative fluorescent speckle microscopy of cytoskeleton dynamics. *Annu Rev Biophys Biomol Struct* 35:361–387.
16. Theriot JA, Mitchison TJ (1991) Actin microfilament dynamics in locomoting cells. *Nature* 352:126–131.
17. Watanabe N, Mitchison TJ (2002) Single-molecule speckle analysis of actin filament turnover in lamellipodia. *Science* 295:1083–1086.
18. Mogilner A, Rubinstein B (2010) Actin disassembly clock and membrane tension determine cell shape and turning: A mathematical model. *J Phys Condens Matter* 22:194118.
19. Kozlov MM, Mogilner A (2007) Model of polarization and bistability of cell fragments. *Biophys J* 93:3811–3819.
20. Grimm HP, Verkhovsky AB, Mogilner A, Meister JJ (2003) Analysis of actin dynamics at the leading edge of crawling cells: Implications for the shape of keratocyte lamellipodia. *Eur Biophys J* 32:563–577.
21. Kovar DR, Pollard TD (2004) Insertional assembly of actin filament barbed ends in association with formins produces piconewton forces. *Proc Natl Acad Sci USA* 101:14725–14730.
22. Bar-Ziv R, Tlusty T, Moses E, Safran SA, Bershadsky A (1999) Pearling in cells: A clue to understanding cell shape. *Proc Natl Acad Sci USA* 96:10140–10145.
23. Holzinger A (2001) Jasplakinolide. An actin-specific reagent that promotes actin polymerization. *Methods Mol Biol* 161:109–120.
24. Nolen BJ, et al. (2009) Characterization of two classes of small molecule inhibitors of Arp2/3 complex. *Nature* 460:1031–1034.
25. Heinemann F, Doschke H, Radmacher M (2011) Keratocyte lamellipodial protrusion is characterized by a concave force-velocity relation. *Biophys J* 100:1420–1427.
26. Theriot JA, Mitchison TJ, Tilney LG, Portnoy DA (1992) The rate of actin-based motility of intracellular listeria monocytogenes equals the rate of actin polymerization. *Nature* 357:257–260.
27. Keren K, Yam PT, Kinkhabwala A, Mogilner A, Theriot JA (2009) Intracellular fluid flow in rapidly moving cells. *Nat Cell Biol* 11:1219–1224.
28. Sinard JH, Pollard TD (1989) Microinjection into *Acanthamoeba castellanii* of monoclonal antibodies to myosin II slows but does not stop cell locomotion. *Cell Motil Cytoskeleton* 12:42–52.
29. Wessels D, et al. (1988) Cell motility and chemotaxis in *Dictyostelium* amebae lacking myosin heavy chain. *Dev Biol* 128:164–177.
30. Lammermann T, Sixt M (2009) Mechanical modes of amoeboid cell migration. *Curr Opin Cell Biol* 21:636–644.
31. Asano Y, et al. (2004) Keratocyte-like locomotion in amiB-null *Dictyostelium* cells. *Cell Motil Cytoskeleton* 59:17–27.
32. Lewis L, et al. (1982) The relationship of fibroblast translocations to cell morphology and stress fibre density. *J Cell Sci* 53:21–36.
33. Cai Y, et al. (2010) Cytoskeletal coherence requires myosin-IIA contractility. *J Cell Sci* 123:413–423.
34. Insall RH, Machesky LM (2009) Actin dynamics at the leading edge: From simple machinery to complex networks. *Dev Cell* 17:310–322.
35. Choi CK, et al. (2008) Actin and α-actinin orchestrate the assembly and maturation of nascent adhesions in a myosin II motor-independent manner. *Nat Cell Biol* 10:1039–1050.
36. Lee J, Jacobson K (1997) The composition and dynamics of cell-substratum adhesions in locomoting fish keratocytes. *J Cell Sci* 110:2833–2844.
37. Pincus Z, Theriot JA (2007) Comparison of quantitative methods for cell-shape analysis. *J Microsc* 227:140–156.

Supporting Information

Ofer et al. 10.1073/pnas.1105333108

SI Text

Actin Network Density Profile from Front-to-Rear. The observed exponential decrease of the actin network density from front-to-rear in lamellipodial fragments (Fig. 2 *C* and *G*) can be easily explained assuming that the actin network disassembles with a constant net rate $1/\tau$. Because the retrograde actin flow with respect to the substrate in fragments is negligible (Fig. 2*E*), we assume that the actin network is flowing rearward in the cell frame of reference with a speed equal to the fragment speed, V (Fig. 2*E*). Thus, the filament density along a cross section perpendicular to the leading edge in the cell frame of reference, $B(s)$, is described by the equation: $\frac{\partial B}{\partial t} = -V\frac{\partial B}{\partial s} - \frac{B}{\tau}$, where s is the distance from the leading edge rearward. The steady-state solution of this equation is

$$B(s) = B_C \exp(-s/V\tau),$$

where B_C is the actin filament density at the center of the leading edge.

Relation Between Front-to-Rear Distance, Speed, and Membrane Tension. The rear boundary within the disassembly clock model is defined by where the actin network has sufficiently disassembled for membrane tension to crush it and translocate the rear boundary (Fig. S10). Let us assume that the mechanical force threshold above which the actin network breaks is proportional to the network density, so there is a certain average force per filament needed to break a filament (or dissociate it from other filaments and/or adhesion complexes). Taking into account the steady-state actin density distribution calculated above, the force balance between the membrane tension and the mechanical force needed to break the actin network at the rear of the fragment can be written as:

$$T = kB(y) = kB_C \exp(-y/V\tau),$$

or following rearrangement as:

$$\exp\left(-\frac{y}{V\tau}\right) = \frac{T}{kB_C} = \frac{f_{\text{stall}}}{k}\frac{T}{f_{\text{stall}}B_C},$$

where T is the membrane tension (force per unit length), k is the breaking force per filament, and y is the front-to-rear distance at the center (all variables and parameters here are dimensional). Note that the total force per unit length applied by the membrane at the boundary is $T = 2\Sigma$, where Σ is the in-plane membrane tension (1). For simplicity we refer to T as the membrane tension.

We introduce two nondimensional parameters,

$$\varepsilon = \frac{f_{\text{stall}}}{k}, \qquad \alpha = \frac{T}{f_{\text{stall}}B_C}, \qquad \textbf{[S1]}$$

where ε is equal to the ratio between the force per filament needed to stall and to break the actin network, whereas α is equal to the force per filament imposed by the membrane tension at the center of the leading edge in units of the stall force. Using these definitions we obtain,

$$\exp(-y/V\tau) = \varepsilon\alpha. \qquad \textbf{[S2]}$$

Note that a more complicated relation between actin network density and the force needed to retract the rear is possible. However, because we find experimentally that the actin network is largely disassembled at the rear (Fig. 2 *C* and *G*), the exact functional form we take between the force and network density is not so important; choosing a linear relation simplifies the math, but other dependence would not change the results substantially. Note also that the force needed to break adhesions with the substrate and deadhere the rear most likely also contributes to the force needed to retract the rear (Fig. S11). Including such contributions obviously complicates the model, but would not change the conceptual picture presented here.

The front corners of the leading edge are defined by where the force per filament is equal to the stall force (Fig. S10). We denote the side-to-side distance by $2x$, so the total length of the front and sides of the leading edge can be approximated by $2L = 2(x+y)$ and the fragment area by $A = 2xy$. At the front corners we have: $B(x)f_{\text{stall}} = B_C\left[1 - \left(\frac{x}{x+y}\right)^2\right]f_{\text{stall}} = T$. Because $x = \frac{A}{2y}$, the last relation can be rewritten as a function of y as, $B_C\left\{1 - \frac{1}{[1+(2y^2/A)]^2}\right\}f_{\text{stall}} = T$. Thus we have,

$$1 - \frac{1}{[1 + (2y^2/A)]^2} = \alpha. \qquad \textbf{[S3]}$$

Substituting Eq. **S3** into Eq. **S2**, we obtain:

$$\exp(-y/V\tau) = \varepsilon\left\{1 - \frac{1}{[1 + (2y^2/A)]^2}\right\}. \qquad \textbf{[S4]}$$

Taking the logarithm of both sides and rearranging we obtain,

$$V = \frac{y}{\tau}\left\{\frac{-1}{\log\varepsilon + \log[1 - (1 + 2y^2/A)^{-2}]}\right\}. \qquad \textbf{[S5]}$$

Thus for a given fragment characterized by the parameters A, ε, τ we obtain a relation between fragment speed and front-to-rear distance. When $\varepsilon = \frac{f_{\text{stall}}}{k} << 1$ is small (i.e., the breaking force is much greater than the stall force) this relation between fragment speed and front-to-rear distance reduces to, $V \approx \frac{y}{\tau}\left(\frac{-1}{\log\varepsilon}\right)$. Note that these results are independent of B_C.

A fragment at steady state is characterized by particular values for the front-to-rear distance and speed and hence can be described as a point in the y-V plane. The local force balance conditions which led to Eq. **S5** have to be met, so this point has to lie on the line defined by the solution to Eq. **S5**. The fragment speed at steady state is equal to the actin protrusion speed at the front. Taking into account the actin polymerization rate and neglecting the off-rate, the protrusion rate can be approximated as,

$$V = k_{\text{eff}}G\varphi(T/B_c), \qquad \textbf{[S6]}$$

where G is the actin monomer concentration, k_{eff} is a proportionality factor which combines the rate of actin polymerization, the partition of actin monomers between profilin and thymosin and other biochemical factors, and $\varphi(T/B_c)$ is the membrane tension-dependent factor which reflects the dependence of the polymerization rate on the force per filament. Because, $\frac{T}{B_C} = \left\{1 - \frac{1}{[1+(2y^2/A)]^2}\right\}f_{\text{stall}}$ (see above), Eq. **S6** leads to another

relation between the front-to-rear distance and speed. The steady-state shape and speed of a fragment are determined as the point of intersection between the line defined by the solution to Eq. **S6** and the line defined by the solution to Eq. **S5** in the y-V plane. In ref. 2, we demonstrated that over a wide range of tension values, $\varphi(T/B_c) \approx 1$, so Eq. **S6** can be further simplified into $V \approx k_{\text{eff}}G$. Thus, in this approximation the protrusion speed at the front is set by the actin monomer concentration, and the front-to-rear distance is determined based on the force balance condition in Eq. **S5**.

We can also evaluate the model predictions by examining the actin network distribution in a large population of fixed fragments. According to the model we expect the actin density decay from front-to-rear to be correlated with the actin distribution along the leading edge. Specifically, from Eq. **S2** and Eq. **S3** we obtain $B_C \exp\left(-\frac{y}{V\tau}\right) = \varepsilon B_s$, which can be rewritten as, $\frac{y}{V\tau} = -\log\varepsilon + \log B_{CS}$, where B_S is the actin density at the front corners and $B_{CS} = B_C/B_S$. Thus, the model predicts a linear relation between the front-to-rear distance (measured in units of the actin density decay length) and the peakedness of the actin distribution along the leading edge characterized by the log of the ratio between the actin density at the center and sides of the leading edge. As shown in Fig. S7, we find good agreement between the data and the model prediction. Furthermore, we obtain an independent estimate for ε from the y-axis intercept in Fig. S7 [$\varepsilon \approx \exp(-1.2) \approx 1/3$], which agrees with the average value calculated based on the dynamics of individual fragments (Fig. 4*B*).

Estimates of Membrane Tension from the Model. For the membrane tension, the theory predicts:

$$\alpha = \frac{T}{f_{\text{stall}}B_c} = 1 - \frac{1}{[1 + 2(y/\sqrt{A})^2]^2}. \qquad \textbf{[S7]}$$

Using this formula, we can estimate the membrane tension for any specific fragment (in units of $f_{\text{stall}}B_C$) from the measured front-to-rear distance and area. The normalized front-to-rear distance $(y/\sqrt{A})$ varies between 0.5 and 1.3 in a population of fragments, so we expect that $0.5 < \alpha < 1$. Assuming, $f_{\text{stall}} \sim 3\ pN$, $B_c \sim 100/\mu\text{m}$, we estimate the membrane tension to be approximately $150 - 300\ \text{pN}/\mu\text{m}$.

Correlation Between Front-to-Rear Distance and Curvature of the Leading Edge. The speed along the leading edge is related to the angular position according to the graded radial extension model (2, 3):

$$V(l) = V(0)\cos\theta(l) \approx V_{\text{cell}}[1 - \theta(l)^2/2], \qquad \textbf{[S8]}$$

where l is the length from the center along the leading edge, and $\theta(l)$ is the angle between the direction of cell movement and the direction of protrusion which is assumed to be locally normal to the leading edge. We denote by R the radius of curvature of the leading edge. For small l, we have $l = \theta(l)R$, so that,

$$V(l) \approx V_{\text{cell}} - l^2\frac{V_{\text{cell}}}{2R^2}.$$

We can expand $V(l)$ into a Taylor series keeping only the lowest order terms,

$$V(l) \approx V(0) + l^2\left.\frac{dV}{d(l^2)}\right|_{l=0}.$$

Given a force-velocity-density relation at the leading edge $V(f)$ and assuming that the force per filament, f, is equal to the membrane tension divided by the local filament density, $f(l^2) = \frac{T}{B(l^2)} = \frac{T}{B_C(1-l^2/L^2)}$, we obtain:

$$\left.\frac{dV}{d(l^2)}\right|_{l=0} = \left.\frac{dV}{df}\frac{df}{d(l^2)}\right|_{l=0} = \left.\frac{T}{B_CL^2}\frac{dV}{df}\right|_{f=T/B_0}.$$

So we can write the Taylor expansion as,

$$V(l) \approx V(0) + l^2\left.\frac{T}{B_CL^2}\frac{dV}{df}\right|_{f=T/B_0}. \qquad \textbf{[S9]}$$

Comparing **[S8]** and **[S9]** we obtain an expression for the curvature of the leading edge:

$$\frac{1}{R} = \frac{1}{L}\sqrt{\left.\frac{2T}{V_{\text{cell}}B_C}\left(-\frac{dV}{df}\right)\right|_{f=T/B_0}}.$$

In ref. 2, we used the following force-velocity-density relation at the leading edge, $V(f) = V_0\left[1 - \left(\frac{f}{f_{\text{stall}}}\right)^w\right]$, where V_0 is the free polymerization rate and $w = 8$. Taking this force-velocity relation we obtain, $\left.\left(-\frac{dV}{df}\right)\right|_{f=T/B_0} = \frac{wV_0B_C}{T}\left(\frac{T}{B_Cf_{\text{stall}}}\right)^w$ so that,

$$\frac{1}{R} = \frac{\sqrt{2w}}{L}\sqrt{\frac{V_0}{V_{\text{cell}}}}\left(\frac{T}{B_Cf_{\text{stall}}}\right)^{w/2}.$$

We approximate the half length of the front and sides of the leading edge as $L = y + A/2y$. The force balance at the front corners of the leading edge where the filaments are stalled can then be written as,

$$B_0\left[1 - \left(\frac{A/2y}{L}\right)^2\right]f_{\text{stall}} = T, \text{ so : } L = \frac{A}{2y\sqrt{1 - \frac{T}{f_{\text{stall}}B_C}}}.$$

Furthermore, $\frac{V_{\text{cell}}}{V_0} = \left[1 - \left(\frac{T}{B_Cf_{\text{stall}}}\right)^w\right]$. Denoting $\alpha = T/B_Cf_{\text{stall}}$ as before we obtain:

$$\frac{1}{R} = \frac{y}{A}\sqrt{\frac{8w(1-\alpha)\alpha^w}{1-\alpha^w}}.$$

Normalizing all the distances to the square root of area we obtain:

$$\tilde{c} = \frac{\sqrt{A}}{R} = \tilde{y}\sqrt{\frac{8w(1-\alpha)\alpha^w}{1-\alpha^w}}.$$

Because $\alpha = \frac{T}{B_Cf_{\text{stall}}} = 1 - \frac{x^2}{L^2} = 1 - \left(\frac{A}{2yL}\right)^2 = 1 - (2\tilde{y}^2 + 1)^{-2}$, we obtain an expression for $\tilde{c}$ as a function of $\tilde{y}$ alone:

$$\tilde{C}(\tilde{y}) = 2\sqrt{2w}\tilde{y}\sqrt{\frac{[1-\alpha(\tilde{y})]\alpha(\tilde{y})^w}{1-\alpha(\tilde{y})^w}}, \alpha(\tilde{y}) = 1 - (2\tilde{y}^2 + 1)^{-2}. \qquad \textbf{[S10]}$$

Fitting our experimental data with this expression gives excellent results (Fig. 5*C*, Fig. S9).

Dynamic Model of Fragment Behavior. One of the central questions in cell motility research is how the lamellipodium sustains its polarity and exhibits persistent motility. We hypothesize that the structure of the actin network which is branched near the

protruding front and bundled at the rear (4) plays a central role in sustaining this asymmetry. We suggest that a positive feedback between the dynamic asymmetric structure of the actin network and its movement sustains protrusion at the leading edge and retraction at the rear. Specifically, we make the following assumptions and show how they lead to such positive feedback. First, there is a limiting number of a molecular branching factor, which is necessary for nucleation of nascent actin filaments and generating protrusions. Second, the presence of nascent actin filaments is essential for localization of the branching factor to protrusions. The mechanism responsible for this requirement could, for example, involve transient attachment of the molecular branching factor to nascent filaments, which is needed for Arp2/3 activation and nucleation of new filaments (5). Third, retraction of the cell edge tends to push filaments against the membrane leading to local actin network deformation, bundling, disassembly and inability to branch. Note that the deformation of the actin network at the trailing edge will be further promoted by myosin filaments which concentrate at the rear because of actin network flow and also promote bundling and disassembly of the actin network near the rear boundary (4, 6).

We hypothesize that as a result of these local mechanisms, global asymmetry in the actin network can arise and persist: When the molecular branching factor focuses on a part of the cell boundary, actin growth in this region leads to local protrusion and generates tension in the membrane. As membrane area is conserved, the tension causes retraction at the opposite edge, which locally depletes the branching factor there. Thus, a mechanical feedback transmitted instantaneously through the membrane acts as a global inhibitor of protrusion and enables focusing local excitatory actin protrusion at the front. The same mechanisms enable the asymmetric actin dynamics, with branching at one end and retraction at the opposite end, to perpetuate and sustain a steady state of actin network treadmilling.

Mathematically, the following model quantifies these qualitative ideas. First, we consider the densities of the right- and left-oriented growing barbed ends along the leading edge, $b^+(l,t)$ $[b^-(l,t)]$, where l is a coordinate along the cell boundary. Following previous work (2, 7), we model these densities with the following equations:

$$\frac{\partial b^{\pm}}{\partial t} = \mp \underbrace{V\frac{\partial b^{\pm}}{\partial l}}_{\text{lateral flow}} + \underbrace{\beta}_{\text{branching}} - \underbrace{\gamma b^{\pm}}_{\text{capping}}.$$

Here V is the lateral flow rate (which is of the order of cell speed) and γ is the constant rate of capping. We assume that the branching rate is proportional to the local density of molecules regulating the branching process, and that this local density is proportional to the local density of the nascent barbed ends to which these molecules bind transiently, so $\beta \sim b^{\mp}$ (note that the right-oriented filaments branch off the left-oriented ones, and vice versa). We further assume that the total number of the branching events at the leading edge is fixed, so the branching term has the following form, $\beta = \frac{\beta_0 b^{\mp}}{B}$, where β_0 is the total number of the branching events per second and $B = \oint [b^+(l,t) + b^-(l,t)]dl$ is the total number of growing barbed ends integrated over the entire cell boundary. Finally, we hypothesize as above, that the barbed end density is zero at the retracting part of the cell edge (Fig. S5): $b^+(l,t) = b^-(l,t) = 0$ if $\vec{V}(l) \cdot \vec{n}(l) < 0$, where $\vec{V}(l)$ is the local edge velocity, and $\vec{n}(l)$ is the respective outward normal unit vector.

The stationary solution for the equations in the previous paragraph (when there is only one connected protruding region along the boundary) has the following form (2, 7):

$$b^+(l) \approx b^-(l) \approx \frac{3\beta_0}{4\gamma L}\left(1 - \frac{4l^2}{L^2}\right),$$

where L is the length of the protruding region and $l = 0$ corresponds to the center of this region. The barbed end density goes to zero at the boundary of the protruding region.

Each fragment is characterized by several parameters (A, τ, ε, B_c, G) corresponding respectively to its area, the characteristic disassembly time, the ratio between the stall force and the breaking force per filament, the actin filament density at the center of the leading edge and the actin monomer concentration. Fragment area is measured and found to be essentially constant in individual fragments over time (variations $< \sim 1\%$; Fig. S2). The parameters τ and ε, which characterize the actin network ultrastructure probably do not vary much within individual fragments so we will assume they remain constant as well. The two parameters that most likely vary over time are the concentration of actin monomers, G, and the density of actin filaments at the center of the leading edge, B_c. In what follows we analyze fragment dynamics under the assumption that these parameters vary over time, but that they change slowly compared to the time of fragment translocation (y/V). As above, we assume that the fragment is approximately rectangular, and its length, y, defines its width:

$$2x = A/y. \qquad \textbf{[S11]}$$

The length of the leading edge in this rectangular geometry is:

$$L = 2x + 2y. \qquad \textbf{[S12]}$$

At the center and sides of the leading edge, the barbed end densities are:

$$B_c = \frac{3\bar{B}}{2L}, B_s = \frac{3\bar{B}}{2L}\left(1 - \frac{x^2}{L^2}\right), \qquad \textbf{[S13]}$$

where $\bar{B}$ is the total number of the growing barbed ends. Finally, the density of actin filaments at the rear is:

$$B_{\text{rear}} = B_c \exp(-y/V\tau), \qquad \textbf{[S14]}$$

and the membrane tension is:

$$T = B_s f_{\text{stall}}. \qquad \textbf{[S15]}$$

The fragment front-to-rear length y is governed by the equation:

$$dy/dt = V_f - V_r, \qquad \textbf{[S16]}$$

where the front and rear velocity are given by the respective force-velocity relations:

$$V_f = \alpha G\left[1 - \left(\frac{T}{f_{\text{stall}} B_c}\right)^w\right], V_r \approx \chi \frac{T}{B_{\text{rear}}}. \qquad \textbf{[S17]}$$

Here α, w, χ are constant parameters. The equation for the front velocity stems from the force-velocity relation (2), whereas we assume that the rate of retraction at the rear is proportional to the force per filament in the actin network at the rear due to membrane tension. Any other tension-density-velocity relation at the rear in which the velocity increases with growing tension and decreases with growing actin density leads to the same qualitative results. For example, a threshold-like relation such that the rear velocity is very large (small) if the membrane tension force per filament is lower (higher) than a threshold works as well. Simple numerical analysis of the differential Eq. **S16** solved

simultaneously with the algebraic Eqs. **S11–S15**, and **S17** demonstrate that this system of equations has a unique stable steady state that corresponds to the static cell shape analyzed above in the framework of the algebraic model.

We hypothesize that fluctuations in the actin monomer concentration are the main source of the observed variations in shape and speed of motile fragments. We suggest that fragment speed varies slowly because of fluctuations in actin monomer concentration. Eqs. **S11–S17** predict that the front-to-rear length will vary in sync with fragment speed as observed experimentally (Fig. 3). Further research is required to determine the expected shape dynamics if the variations in actin monomer and network distributions are not slow compared to the time of fragment translocation and/or if variations in actin disassembly time or breaking force contribute significantly.

This model of self-organization and polarity maintenance is highly speculative; further research is needed to identify the molecular branching factor and to test its dynamics and kinetics. Our goal in this paper is more limited—to illustrate the global role of membrane tension as a mechanical regulator connecting the front and rear of motile cells. Although it is obvious that membrane tension and the treadmilling actin network's structure contribute to the persistent asymmetry apparent in lamellipodial motility, it is still unclear whether this essentially mechanical feedback is sufficient or if biochemical signaling is essential.

SI Materials and Methods

Cell Culture and Fragment Induction. Primary cultures are prepared from the Central American cichlid *Hypsophrys nicaraguensis*. Scales are plucked from the fish body, sandwiched between two glass 22-mm coverslips and cultured at room temperature in Leibovitz's L-15 media (Gibco BRL), supplemented with 14.2 mM Hepes pH 7.4, 10% FBS (Invitrogen), and 1% antibiotic-antimycotic (Gibco BRL). Sheets of keratocytes that migrate off the scale after 16–24 h are detached and disaggregated into individual cells by treatment with 0.1% trypsin (Gibco BRL) with 1 mM EDTA in PBS for 6 min. Addition of 10× volume of culture media quenches the trypsin, and the cells are replated onto a new coverslip. Cell fragment formation is induced 1–5 h after replating by incubation in 1 mL of culture media supplemented with 100 nM staurosporine (Sigma) at 35 °C for 30 min with the lid half open. Cells and fragments are washed in normal media and allowed to recover for at least 10 min prior to observation on the microscope. Measurements extracted from time-lapse observations and correlation analysis of (rare) naturally occurring fragments could not be distinguished from measurements of induced fragments formed according to this protocol. Furthermore, keratocyte populations examined in culture media after recovery from the staurosporine treatment were similar to cell populations gathered from untreated cultures (Fig. S1).

Pharmacological treatments are done by adding to the culture media 50–100 μM blebbistatin (active enantiomer, Sigma), 0.5 μM jasplakinolide (Invitrogen), 100 μM Arp2/3 inhibitor (CK-666, ChemDiv), or 10 μM focal adhesion kinase (FAK) inhibitor (TOCRIS bioscience). High osmolarity media is prepared by adding sorbitol (Sigma) to the normal culture media at a final total osmolarity of 600 ± 5 mOsm (compared to 315 ± 5 mOsm for normal culture media). Perturbation experiments are done by imaging individual cells or fragments for approximately 10 min prior to the perturbation followed by 10–20 min after the perturbation.

Fixation and Staining of Actin. Cells are fixed with 4% formaldehyde (Sigma) in cytoskeleton buffer (10 mM MES pH 6.1, 117 mM KCL, 3 mM MgCl2 and 2 mM EGTA) supplemented with 320 mM sucrose for 15 min. The samples are washed with PBS, permeabilized with PBS+0.5% Triton X100 (Sigma) for 10 min followed by incubation in PBS-BT (PBS with 0.1% TX100 and 3% BSA) for 10 min. Cells are stained with Alexa-Fluor-488 phalloidin (2 u/mL; Invitrogen) in PBS-BT, washed and mounted in 10 mM phenylenediamine, 1 mg/mL n-propyl-gallate (Sigma), 90% glycerol in PBS.

Microscopy. Live cell imaging is performed on glass-bottom petri dishes (fluorodish; World Precision Instruments Ltd.) at room temperature on a Zeiss Axio-Observer inverted microscope and acquired using a CoolSnap HQ2 CCD camera (Photometrics). Fragment and cell population data are acquired by imaging individual fragments or cells three times, every 30 s, using a $63\times$ objective (N.A. = 1.4) with a $1.6\times$ optovar. Time-lapse imaging is done at 3 s intervals using a $63\times$ objective (N.A. = 1.4). Fixed fragments or cells are imaged using a $63\times$ objective (N.A. = 1.4) with a $1.6\times$ optovar.

Measurements of Net Actin Disassembly Rates. Time-lapse imaging is done on live fragments at 3 s intervals over 10 min as described above, and immediately followed by formaldehyde fixation and phalloidin staining. The same fragment is identified and imaged before and after fixation and staining of the sample. The actin network distribution along a cross section perpendicular to the leading edge is averaged over an approximately 2-μm wide stripe. The actin network density is fit to an exponential decay $B(s) = B_C \exp(-s/\lambda)$, with the decay length λ as a fit parameter. The fit region is taken to be from 1 μm behind the leading edge until 2 μm before the trailing edge. The net actin disassembly rate is calculated as $\tau = \lambda/\langle V \rangle$, where $\langle V \rangle$ is the average fragment speed prior to fixation.

Fluorescence Speckle Microscopy. We use the procedure developed by Yam et al. (8), in which low levels of AlexaFluor-546-phalloidin (Invitrogen) are used to visualize actin dynamics in live cells. Four micromolars fluorescent phalloidin is premixed with 20 μM dNTPs (each) in water and incubated for approximately 15 min at room temperature to prevent aggregation. Cells are electroporated with 20 μL of the phalloidin mixture with three pulses at 150 V and are then allowed to recover for approximately 10 min. Fragmentation is induced as above before viewing on a Zeiss Axio-Observer inverted microscope using a $63\times$ objective (N.A. = 1.4) with a $1.6\times$ optovar. Time-lapse phase-contrast and fluorescence movies are acquired using a QuantEM CCD camera (Photometrics). Analysis of actin network flow field in the lab and cell frame of reference is done as described previously (6, 8).

Quantitative Image Analysis. Cell morphology is measured by representing cell shapes as polygonal outlines. The shape modes are calculated by principal components analysis as described previously (2, 9). Briefly, cell contours are manually traced using the magnetic lasso tool in Adobe Photoshop. Outlines are extracted from the masks to derive a series of 200 (x, y) points, evenly spaced along the cell boundary. The outlines are mutually aligned to bring the shapes into a common reference frame as described in refs. 2 and 9 using the contour points and an additional manually defined landmark point at the center of the leading edge. Measured characteristics include: area, front-to-rear distance, curvature of the leading edge, and speed. Area is measured directly from the polygons with the standard formula. Front-to-rear distance is measured as the distance between the center front and rear points along the aligned contours. The radius of curvature of the leading edge is calculated as the radius of the least-squares geometric fit of a circle to the points corresponding to the forward 40% of the cell perimeter. Speed for the live population data is extracted from the displacement of the centroid as determined from the manually drawn masks of the images taken 30 s apart. For time-lapse movies of individual fragments, we measure the speed perpendicular to the boundary at the center of the leading edge and of the trailing edge. The mean fragment speed is

taken as the average of the front and rear edge speed. All the speed data from the time-lapse movies is smoothed using a Gaussian-weighted moving average ($\sigma = 6$ s). A qualitative measure of the relative actin density near the leading edge is obtained from the background subtracted intensity of the inverted phase-contrast images.

The cross-covariance functions are determined by calculating the cross-correlation as a function of time lag between pairs of mean-subtracted time series describing different properties of individual fragments. For each fragment at least 200 time points at 3 s time intervals are used. The cross-covariance functions are normalized so that the auto-covariances at zero time lags are equal to one.

The actin distribution along the fragment boundary and along a cross section perpendicular to the leading edge is measured following fixation and phalloidin staining. The distribution of actin filament density along the boundary is calculated by averaging the intensity of background-corrected fluorescence images between 1 and 2 μm from the cell edge along the boundary. The distribution perpendicular to the leading edge is averaged over 10 contour points (out of 200 contour points) around the center along the cross section.

1. Kovar DR, Pollard TD (2004) Insertional assembly of actin filament barbed ends in association with formins produces piconewton forces. *Proc Natl Acad Sci USA* 101:14725–14730.
2. Keren K, et al. (2008) Mechanism of shape determination in motile cells. *Nature* 453:475–480.
3. Lee J, Ishihara A, Theriot JA, Jacobson K (1993) Principles of locomotion for simple-shaped cells. *Nature* 362:167–171.
4. Svitkina TM, Verkhovsky AB, McQuade KM, Borisy GG (1997) Analysis of the actin-myosin II system in fish epidermal keratocytes: Mechanism of cell body translocation. *J Cell Biol* 139:397–415.
5. Co C, Wong DT, Gierke S, Chang V, Taunton J (2007) Mechanism of actin network attachment to moving membranes: Barbed end capture by N-WASP WH2 domains. *Cell* 128:901–913.
6. Wilson CA, et al. (2010) Myosin II contributes to cell-scale actin network treadmilling through network disassembly. *Nature* 465:373–377.
7. Lacayo CI, et al. (2007) Emergence of large-scale cell morphology and movement from local actin filament growth dynamics. *PLoS Biol* 5:e233.
8. Yam PT, et al. (2007) Actin-myosin network reorganization breaks symmetry at the cell rear to spontaneously initiate polarized cell motility. *J Cell Biol* 178:1207–1221.
9. Pincus Z, Theriot JA (2007) Comparison of quantitative methods for cell-shape analysis. *J Microsc* 227:140–156.

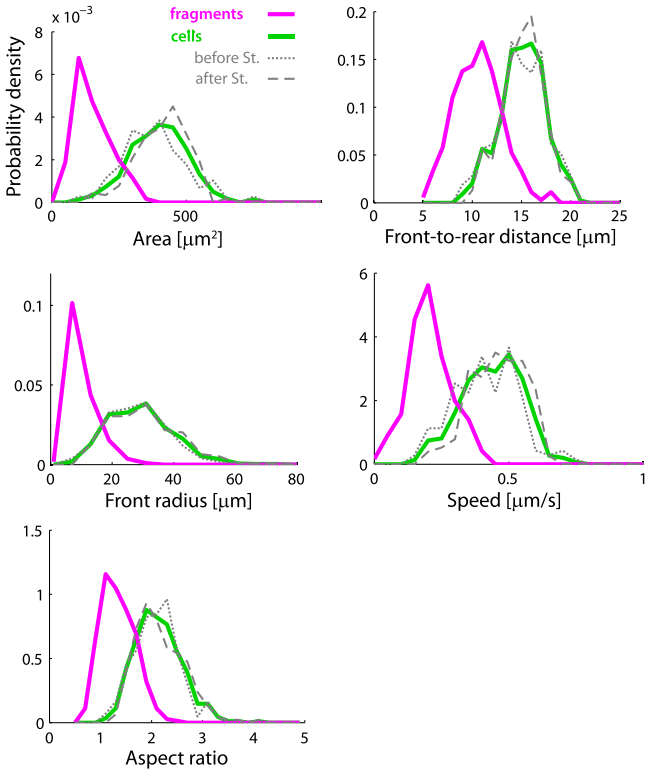

Fig. S1. The distribution of morphological characteristics and speed in populations of fragments and cells. The distributions of area, front-to-rear distance, radius of curvature of the leading edge, speed and aspect ratio are shown for a population of live fragments ($N = 122$, magenta) and cells ($N = 148$, green). The distributions for cells before and after treatment with staurosporine to induce fragmentation (see *Materials and Methods*) are also shown separately (dotted and dashed gray lines, respectively). The distributions before and after treatment are essentially the same, indicating that there are no measurable changes in cell behavior following the protocol used to induce fragmentation.

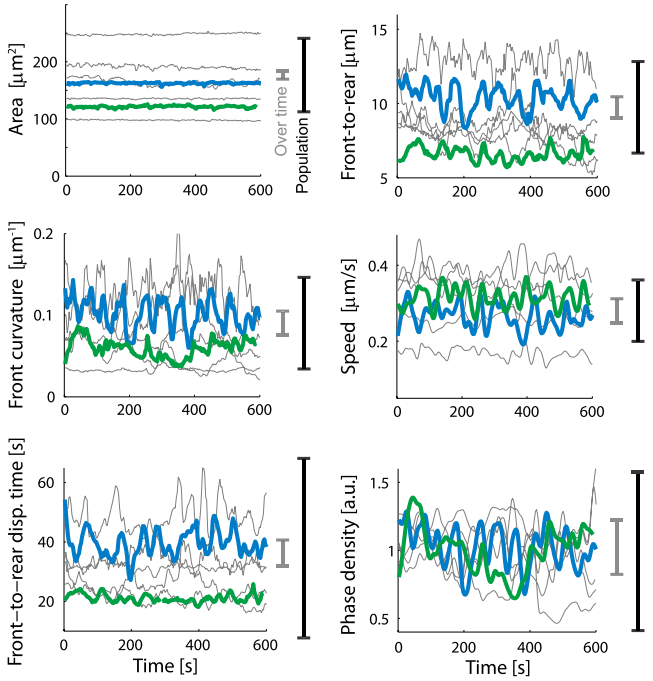

Fig. S2. Natural variation in fragment shape and speed within individual fragments over time. Fragments were imaged by time-lapse phase-contrast microscopy for at least 10 min at 3 s intervals. Traces of area, front-to-rear distance, front curvature, speed, front-to-rear displacement time (i.e., the front-to-rear distance divided by speed) and phase density at the leading edge center are shown as a function of time for seven different fragments (out of 45 fragments followed overall). The green and blue lines refer to the two fragments shown in Fig. 3*A*. Area remains nearly constant, whereas other properties exhibit larger variation over time. The extent of variation within individual fragments and in the population for each property measured is indicated by the lines to the right of each graph. The length of the gray lines is equal to twice the average (over all 45 fragments) of the standard deviation of each property over 10 min within individual fragments. The length of the black lines is equal to twice the standard deviation of that property in a population of fragments ($N = 122$, see Fig. S1).

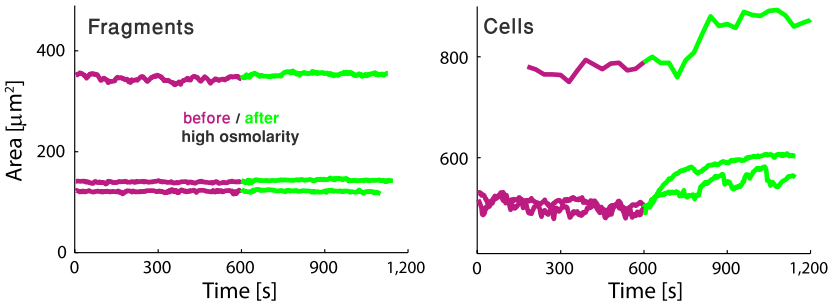

Fig. S3. Fragment area remains constant following high osmolarity perturbation. Fragments and cells were imaged by time-lapse phase-contrast microscopy before and after changing the medium from normal cell culture media (315 ± 5 mOsm) to high osmolarity media (600 ± 5 mOsm). Graphs of area over time for different fragments (*Right*) and cells (*Left*) before and after switching to high osmolarity media are shown. Although fragments maintain constant area regardless of the perturbation, cells exhibit substantial changes in area in response to the increased osmolarity. The initial increase in area in cells is at least partly due to membrane moving from around the shrinking cell body and into the lamellipodium in response to the perturbation.

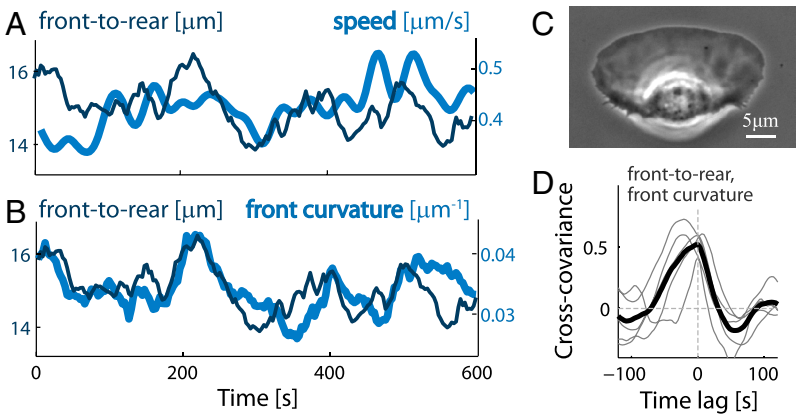

Fig. S4. Correlations in shape and speed within individual keratocytes over time. Cells were imaged by time-lapse phase-contrast microscopy for at least 10 min at 3 s intervals. (*A* and *B*) Traces of the front-to-rear distance and cell speed (*A*) and the front-to-rear distance and the curvature of the leading edge (*B*) over time are depicted for an individual cell. The front-to-rear distance is correlated with both speed and front curvature. (*C*) Phase-contrast image of the cell analyzed in *A* and *B*. (*D*) The normalized cross-covariance between the front-to-rear distance and the front curvature is depicted as a function of time lag for five individual cells (gray lines), together with the mean cross-covariance function averaged over all cells (black line).

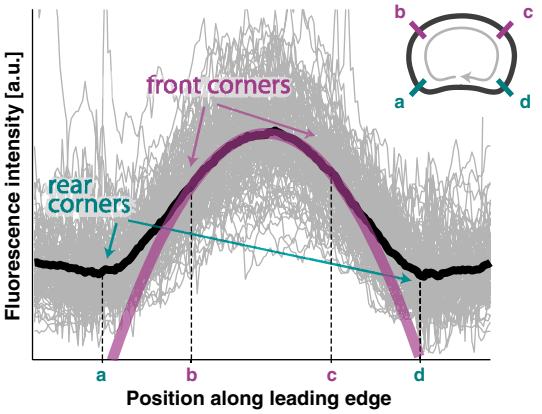

Fig. S5. Actin filament distribution along the leading edge is well-fit by a parabola. The actin filament distribution was measured for a population of fixed fragments ($N = 115$, Fig. 2 *A*–*C*). The actin filament density profile is plotted as a function of the relative position along the fragment boundary (*Inset*). The background subtracted fluorescence intensity in each fragment was normalized to the mean intensity within that fragment. Data for individual fragments (gray lines) is shown together with the population average (black). The mean actin filament density profile along the leading edge (between the front corners; *b* and *c*) is well-fit by a parabola (purple line) that goes to zero approximately at the rear corners (*a* and *d*).

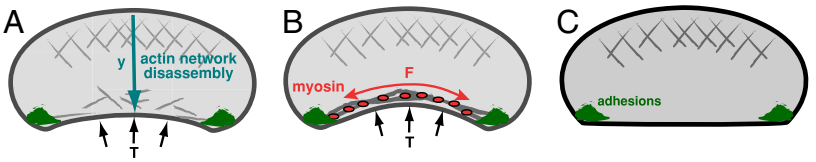

Fig. S6. Possible models for rear lamellipodial shape determination. (*A*) The rear shape is set by a disassembly clock as explained in the text. (*B*) The rear boundary is shaped by a balance between membrane tension, T, and the force of myosin contraction/actin elasticity, F, along the boundary. The rear radius is determined according to Laplace law: $R_{rear} = F/T$. (*C*) The membrane is stretched taut between the adhesion sites at the rear corners of the fragment.

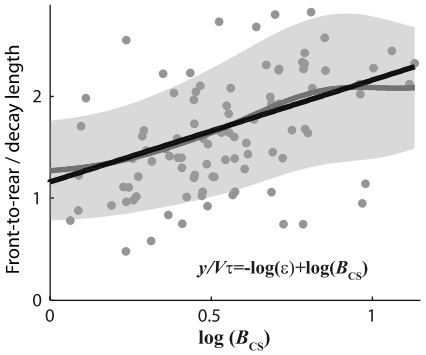

Fig. S7. The actin density decay from front-to-rear is correlated with the peakedness of the actin distribution along the leading edge. The ratio between the front-to-rear distance and the characteristic decay length of the actin density from front-to-rear is plotted as a function of the log of the ratio between the actin density at the center and sides of the leading edge for a population of fixed fragments ($N = 115$). Each data point represents an individual fragment. The prediction of the disassembly clock model: $\frac{y}{V\tau} = -\log\varepsilon + \log B_{CS}$ (black line), captures the mean trend in the data plotted as a Gaussian-weighted moving average ($\sigma = 0.15$, gray line) ± one standard deviation (shaded region).

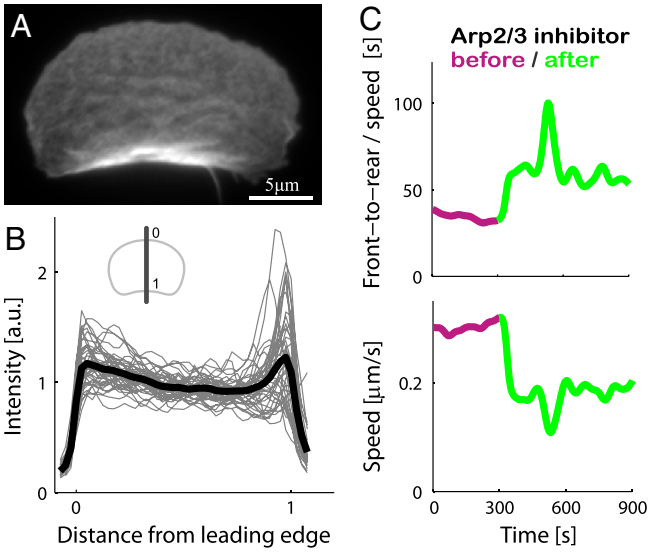

Fig. S8. The effect of Arp2/3 inhibition on fragments. (*A*) A fluorescence image of a fragment which was fixed and stained with fluorescent phalloidin 10 min after addition of an Arp2/3 inhibitor. Note the qualitative difference in the actin network organization compared to untreated fragments (Fig. 2*A*). (*B*) The actin filament distribution was measured for a population of fixed fragments ($N = 45$) following treatment with an Arp2/3 inhibitor as in *A*. The background subtracted fluorescence intensity in each fragment was normalized to the mean intensity within that fragment. The density along a cross section perpendicular to the leading edge is plotted as a function of the normalized distance from the leading edge (front-to-rear distance = 1). Data for individual fragments (gray lines) is shown together with the population average (black). The decay of the actin filament density from front-to-rear is markedly slower than in untreated fragments (Fig. 2*C*). (*C*) The speed and front-to-rear displacement time (equal to the front-to-rear distance divided by speed) are depicted as a function of time for a fragment before and after adding the Arp2/3 inhibitor to the media. The front-to-rear displacement time which is nearly constant prior to the perturbation increases following the addition of the Arp2/3 inhibitor, whereas speed decreases in response to the perturbation. These results are aligned with the predictions of the disassembly clock model given the lower actin filament density at the leading edge and the slower network disassembly. Similar results were obtained for three different fragments.

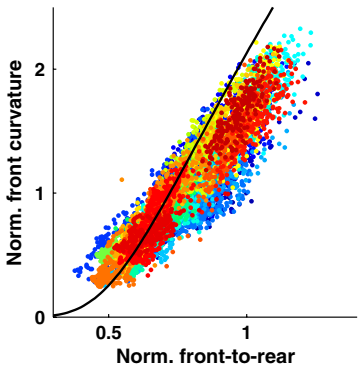

Fig. S9. Front curvature and front-to-rear distance are correlated. The normalized front curvature is shown as a function of the normalized front-to-rear distance. Normalization is done by using the square root of the fragment area as the length unit. Data (as in Fig. 5*C*) is shown for 45 different live fragments. Data from each fragment is depicted in a different color. The solid line gives the model prediction (see *SI Text* for details) which compares well with data.

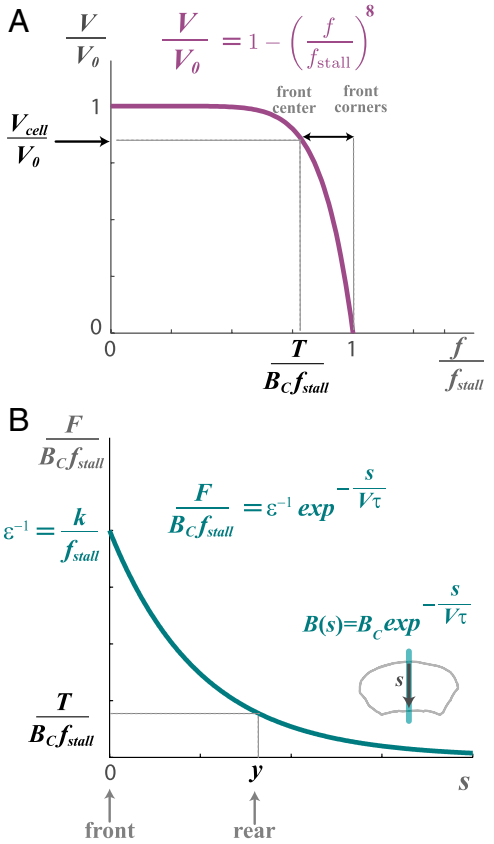

Fig. S10. Force balance along the boundary. (*A*) Leading edge. The normalized force-velocity relation for the actin network along the leading edge is shown. Protrusion rate in units of the free polymerization rate is shown as a function of the force per filament in units of the stall force. The black arrow indicates the range of forces experienced along the leading edge of a fragment with B_C filaments at the center leading edge and tension T. The minimal force, $T/B_C f_{stall}$, is experienced at the center where filament density is highest, and this force determines cell speed. The force per filament increases toward the sides and reaches the stall force for actin polymerization at the front corners of the fragment. (*B*) Trailing edge. The force needed to crush the network in units of stall force per filament at the leading edge is shown as a function of the perpendicular distance from the leading edge(s). The rear of the cell ($s = y$) is defined by where the force needed to crush the network equals the membrane tension.

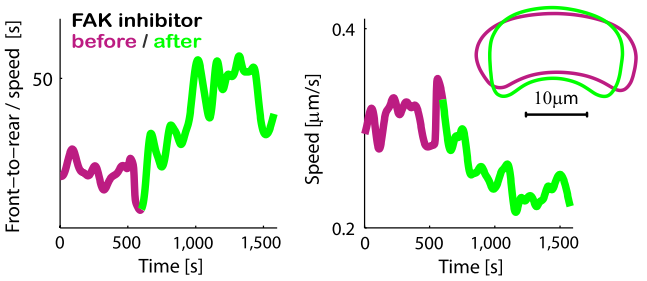

Fig. S11. The effect of FAK inhibition on fragments. The speed and front-to-rear displacement time (equal to the front-to-rear distance divided by speed) are depicted as a function of time for a fragment before and after adding FAK inhibitor to the media. The front-to-rear displacement time which is nearly constant prior to the perturbation increases following the addition of the inhibitor, whereas speed decreases in response to the perturbation. Inhibition of FAK likely slows down turnover of adhesion complexes making it harder to retract the rear. The effect of slower deadhesion is similar to the effect of slowing actin disassembly with jasplakinolide (Fig. 4*C*); the time required for sufficient disassembly of actin and adhesions becomes longer leading to increased tension, lower speed, and larger front-to-rear displacement time. Similar results were obtained for four different fragments.

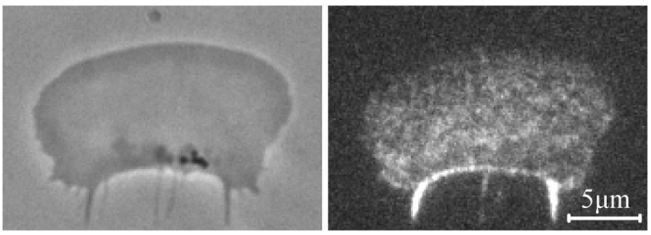

Movie S1. This movie shows phase-contrast (*Left*) and fluorescence (*Right*) images of a keratocyte fragment labeled with low levels of 546 AlexaFluor conjugated phalloidin to visualize actin network dynamics. The movie is shown in the frame of reference of the moving fragment. The measured actin network flow fields for this fragment are shown in Fig. 2*E*. Images were taken every 3 s and the movie is shown at 18 × real time. The field of view is 24-μm wide.
Movie S1 (MOV)

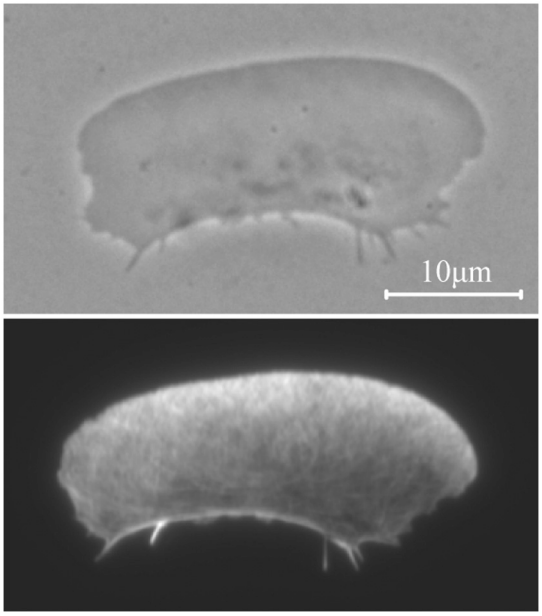

Movie S2. This movie shows phase-contrast images of a live keratocyte fragment that was subsequently fixed and labeled with 488 AlexaFluor conjugated phalloidin to visualize its actin network distribution. Measurements of the actin disassembly time extracted from this movie are shown in Fig. 2*G*. The field of view is 54-μm wide. Images were taken every 3 s prior to fixation, and the movie is shown at 24 × real time.
Movie S2 (WMV)

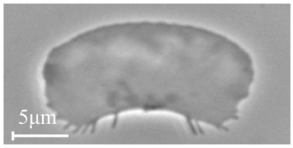

Movie S3. This movie shows phase-contrast images of a round keratocyte fragment (Fig. 3*A*, *Top*). The field of view is 138-μm wide. Images were taken every 3 s, and the movie is shown at 18 × real time.
Movie S3 (MOV)

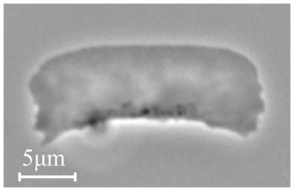

Movie S4. This movie shows phase-contrast images of an elongated keratocyte fragment (Fig. 3*A*, *Bottom*). The field of view is 138-μm wide. Images were taken every 3 s, and the movie is shown at 18 × real time.
Movie S4 (MOV)